Corrosion Science 90 (2015) 420–433

Contents lists available at ScienceDirect

Corrosion Science

journal homepage: www.elsevier.com/locate/corsci

Influence of temperature on the atmospheric corrosion of the Mg–Al alloy AM50

M. Esmaily [a,*], M. Shahabi-Navid [a], J.-E. Svensson [a], M. Halvarsson [b], L. Nyborg [c], Y. Cao [c], L.-G. Johansson [a]

[a] Department of Chemical and Biological Engineering, Chalmers University of Technology, SE-412 96 Göteborg, Sweden
[b] Department of Applied Physics, Chalmers University of Technology, SE-412 96 Göteborg, Sweden
[c] Department of Materials & Manufacturing Technology, Chalmers University of Technology, 2A, SE-412 96 Göteborg, Sweden

ARTICLE INFO

Article history:
Received 8 January 2014
Accepted 26 October 2014
Available online 4 November 2014

Keywords:
A. Magnesium
A. Alloy
B. SEM
C. Atmospheric corrosion

ABSTRACT

The effect of temperature on the NaCl-induced atmospheric corrosion of the Mg–Al alloy AM50 has been investigated in the laboratory. The corroded samples were analyzed gravimetrically and by SEM, EDX, XRD, and FTIR. The atmospheric corrosion of 99.97% Mg was also studied for reference. While the NaCl-induced atmospheric corrosion of AM50 is strongly reduced with decreasing temperature, 99.97% Mg does not exhibit such a trend. The temperature dependence of the atmospheric corrosion of alloy AM50 is attributed to the aluminum content in the alloy. Several crystalline magnesium hydroxy carbonates formed at 4 and 22 °C but were absent at −4 °C.

1. Introduction

Magnesium–aluminum (Mg–Al) alloys are widely used as structural materials, *e.g.*, in the aerospace and automotive industries as a result of their light weight, good castability and good mechanical properties at room temperature. However, the use is limited by their relatively poor corrosion resistance [1–8]. In general, the corrosion properties of Mg–Al alloys rely on the properties of the partially protective surface film which is made up mainly of $Mg(OH)_2$ but which also contains Al^{3+} [9,10]. It is known that the corrosion of Mg and its alloys in aqueous solution is an electrochemical process where magnesium dissolves anodically, the dominant cathodic reaction being hydrogen evolution [11–16]. The partially protective surface film is an electronic insulator and the rate of corrosion is strongly accelerated by the presence of cathodically active surfaces such as noble precipitates in the alloy (*e.g.*, MgFe intermetallics) [2,17–21]. Consequently, the concentration of selected impurities (*e.g.* Fe) is kept below certain limits in commercial alloys in order to avoid forming such precipitates.

Because Mg–Al alloys are often used in atmospheric conditions a better understanding of the atmospheric corrosion properties is of great importance. Accordingly, the atmospheric corrosion properties of Mg and Mg–Al alloys under outdoor conditions have been widely investigated [22–26]. The atmospheric corrosion of Mg–Al alloys has also been investigated under controlled conditions in the laboratory, *e.g.*, in order to investigate the mechanism of corrosion and the influence of various parameters on corrosion [27–36]. It has been reported that while the rate of corrosion when immersed in aqueous solutions or subjected to salt spray tests is high in comparison to other engineering alloys, the corrosion rates of Mg–Al alloys in the outdoor atmosphere are comparable to mild steel. The causes behind the relatively slow atmospheric corrosion of Mg–Al alloys are still not fully understood [10,27]. It is suggested that the inhibitive effect of ambient concentrations of CO_2 on the corrosion of Mg and, Mg–Al alloys reported by [28] and further investigated in a recent study [29] may be part of the explanation.

The corrosion of both Mg and Al in aqueous solution is known to be accelerated by chloride ions [12,18]. Hence, the deposition of chlorides in particulate form (*e.g.* sea salt) is an important factor in the atmospheric corrosion of Mg–Al alloys. In large parts of the world where deicing salt is used, the exterior of cars are heavily exposed to NaCl during winter. Considering that there may be significant NaCl-induced atmospheric corrosion of Mg–Al alloys in automotive applications at temperatures close to or below 0 °C, it is surprising that little scientific work has been devoted to atmospheric corrosion of Mg–Al alloys in that temperature range. Instead, most investigations of atmospheric corrosion in the laboratory are carried out at room temperature or above (*e.g.* in salt spray testing).

Even when other metallic materials are included, investigations of atmospheric corrosion below ambient temperature are relatively few, especially at sub-zero temperatures [37–40]. Working

* Corresponding author. Tel.: +46 317722864.
E-mail address: mohsen.esmaily@chalmers.se (M. Esmaily).

http://dx.doi.org/10.1016/j.corsci.2014.10.040
0010-938X/

with aluminum at 4–60 °C, Blücher et al. [37] reported on a very strong positive correlation between temperature and the rate of NaCl-induced corrosion in humid air. In contrast, Niklasson et al. [38] reported that the atmospheric corrosion of lead in the presence of gaseous acetic acid exhibited a negative correlation with temperature (4 and 22 °C). Also, Svensson and Johansson [39] reported on a negative correlation with temperature (4 and 22 °C) in the case of SO_2-induced atmospheric corrosion of zinc at high relative humidity. Recently, Chen et al. [40] reported on a positive correlation between corrosion attack and temperature for the initial stages (2 h) of NaCl-induced atmospheric corrosion of the Mg–Al alloy AZ91 between 2 °C and 8 °C. The work was carried out in pure water vapor at about 0.01 atm and only investigated the initial attack (2 h).

The present paper is the first attempt to investigate the temperature dependence of the atmospheric corrosion of an Mg–Al alloy down to sub-zero temperatures. Thus, the NaCl-induced atmospheric corrosion of the Mg–Al alloy AM50 is investigated at 22, 4 and −4 °C. In order to study the effect of temperature rather than the combined effects of temperature and relative humidity, all exposures are carried out at a constant relative humidity of 95%. In addition, we report on the influence of ambient levels of CO_2 on corrosion behavior. 99.97% Mg is used as a reference material and comparisons are made to samples exposed in the absence of NaCl.

2. Experimental

2.1. Sample preparation

Chemical compositions of the tested materials, namely pure Mg (99.97%) and alloy AM50, are listed in Table 1. Unalloyed Mg (99.97% Mg) was used as reference material. As-received material was machined to obtain $14 \times 14 \times 3$ mm^3 test coupons with an exposed surface area of 5.56 cm^2 from high purity Mg and High Pressure Die Cast (HPDC) AM50 alloy. Prior to the exposures, samples were ground, lubricated with de-ionized water, through successive grades of silicon carbide abrasive papers (SiC grit papers) from P1000 to P4000 mesh. Polishing was then performed using cloth discs and diamond paste in the range of 1–3 μm, followed by a fine polishing step using oxidized porous silicon (OPS) for 120 s on a Buehler Microcloth. The specimens were cleaned using distilled water and degreased with acetone, washed again with distilled water, and dried with a blower (cool air) and stored in a desiccator over a desiccant for 24 h (h) before exposure. A solution of 20 ml distilled water, 80 ml ethanol and 1 g NaCl was sprayed on the test coupons. The samples were contaminated with two different amounts of salt, 14 and 70 μg/cm^2. Care was taken to avoid an uneven distribution of NaCl on the specimen surface by the spraying of the NaCl solution.

In order to achieve an even distribution of salt, the spraying procedure was optimized with respect *e.g.* to the distance between the spray gun and by dividing the spraying into several steps with intermittent drying. Also, reference samples, i.e. samples without salt, were exposed at the same time with the contaminated samples in each corrosion condition. Duplicate and triplicate samples were exposed for each condition and some of the experiments were repeated several times to check for consistency. In total about 450 samples were exposed.

2.2. Experimental set-up

The experimental set-up for the exposures with 400 ppm CO_2 has been described in detail previously [27,28]. The exposure apparatus is entirely made in glass and Teflon. The samples are suspended by a nylon string in individual exposure chambers. The gas flow is 1000 ml/min corresponding to an average flow velocity of 1 mm/s. Relative humidity (RH) is regulated by mixing measured amounts of dry air and air saturated with water vapor at the exposure temperature. RH was 95 ± 0.3%. CO_2 is added from a cylinder to give a constant concentration of 400 ± 20 ppm. The amount of CO_2 added was measured before and after the experiment. To perform corrosion experiment at sub-zero temperature, a new corrosion system was designed and developed, as illustrated in Fig. 1. Ethylene glycol was used as antifreeze. In addition, two internal humidifiers were placed inside the liquid of the pool to decrease the dew point of the humidified air to −4 °C.

The corrosion exposures in the absence of CO_2 were carried out in hermetically closed desiccators (as corrosion reactors) with a volume of 3dm^3. Exposure temperatures were 22.00 ± 0.03 °C 4.00 ± 0.03 °C and −4.00 ± 0.03 °C. The 95% humid air was achieved by equilibrating with 500 ml potassium hydroxide solution (KOH (aq)) in a container placed inside the desiccator. The water vapor partial pressure over KOH (aq) was calculated by the equation reported in [41]. In addition to the RH to the desired value, i.e. 95%, the KOH (aq) solution also functions as a CO_2 absorbent.

2.3. Quantitative measurements

2.3.1. Gravimetric measurement

To monitor the atmospheric corrosion process the test coupons were removed from reactors during the exposures for weighing with regular intervals except for the CO_2-free exposures, i.e. desiccator exposures. Therefore, the water contained in the NaCl electrolyte remains during weighing and the corresponding mass gains are accordingly called wet mass gains. At the conclusion of an exposure, after measuring the wet mass, the samples were stored for 24 h at room temperature over a desiccant so that the loosely bound water was removed. The specimens were weighed again and the corresponding mass gains are termed dry mass gains.

2.3.2. Leaching and pickling

The quantity of corrosion product was determined via leaching and pickling processes of the corroded specimens using agitating ultrasonic bath at room temperature. The water soluble corrosion products and unreacted NaCl were first removed by leaching process. To do this, the samples were immersed in Mili-Q water (ultrapure water) in two steps; 30 s and 60 s at 25 °C. Subsequently, the corroded samples were pickled several times in a chromate solution of 20% chromium trioxide (CrO_3) for 15 s followed by several periods of 30 s. The heavily corroded samples were pickled up to 25 times. The samples were cleaned by pure water and acetone and finally dried by a stream of cold air after each step. The weight of the samples was registered after each leaching and pickling process to monitor the removal process of the corrosion products. The metal loss was determined by weighing the samples after leaching and pickling. It is noticed that self-corrosion during pickling was negligible. Quantitative data

Table 1
Composition of the test materials (% by weight).

	Al	Zn	Mn	Si	Fe	Cu	Ni	Ca
Mg	0.0030	0.0050	0.0023	0.0030	0.0018	0.0003	0.0002	0.0010
AM50	5.0	0.01	0.25	0.01	0.0016	0.0010	0.0007	n.a.

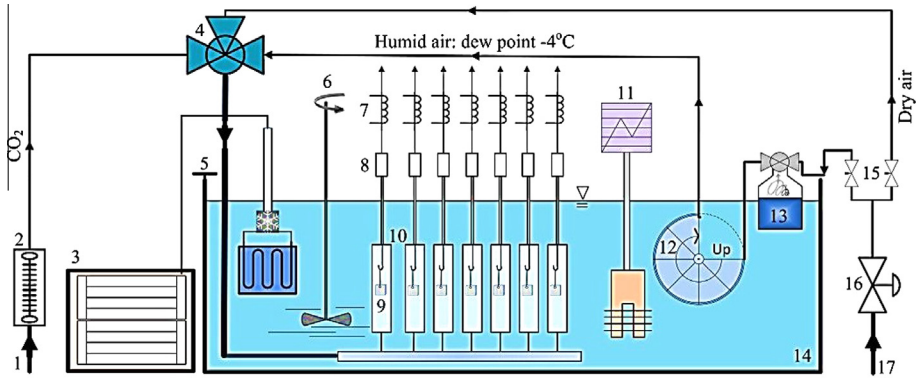

Fig. 1. Schematic diagram of the exposure chamber for the sub-zero atmospheric corrosion experiment: (1) CO_2 source, (2) flow meter, (3) dip cooler, (4) mixing chamber, (5) insulation, (6) stirrer, (7) solenoid valves, (8) wash bottles, (9) corrosion samples suspended by nylon string, (10) corrosion chambers, (11) temperature regulator, (12 and 13) humidifiers producing 95% RH air at the exposure temperature (−4 °C), (14) water +44% ethylene glycol at constant temperature, (15) needle valves, (16) manometer valve (17) dry purified air with a pressure of 6 bars.

on corrosion product stoichiometry were obtained by calculating the corrosion product ratio according to the following equations:

$$M_{\text{loss}} = (M_O) - (M_P) \quad (1)$$

$$M_{\text{Corr}} = (M_{\text{Dry}}) - (M_P) \quad (2)$$

$$X = (M_{\text{Corr}}) - (M_{\text{loss}}) \quad (3)$$

where M_{loss} is metal loss, M_O is mass before exposure and salt, M_P is mass after final stage of pickling, M_{Corr} is mass of corrosion product, M_{Dry} is dry mass and X specifies corrosion product ratio. It should be mentioned that the gravimetric values were averaged from the data (3–8 samples for each test condition) with error bars based on one standard deviation. Some of the exposures were repeated and in total 700 samples were prepared, sprayed, exposed and analyzed to different levels. All gravimetric data were obtained using a Sartorius Microbalance with a with 0.0001 mg resolution.

2.4. Analytical techniques

2.4.1. X-ray diffraction (XRD)

Crystalline corrosion products formed under various exposure conditions were analyzed by X-ray diffraction (XRD) using a Bruker AXS D8 powder diffractometer. The system was equipped with grazing incidence beam attachment and a Göbel mirror. Cr Kα radiation (λ = 2.29 Å) was used and the angle of incidence was 5°.

2.4.2. Fourier transform infrared spectroscopy (FTIR)

In addition to XRD, the corrosion products were also analyzed by Fourier transform infrared (FTIR) spectroscopy. The investigations were conducted from 4000 to 400 cm^{-1} to identify the functional groups in the corrosion products. The FTIR spectrometer used in this study was a Nicolet Magna-IR 560 equipped with a PTGS detector with an insert cell for diffuse reflectance spectroscopy.

2.4.3. Analytical scanning electron microscope (SEM/EDX)

The morphology of the corrosion products was examined by an FEI Quanta 200 environmental scanning electron microscopy (ESEM) with a Schottky field emission gun (FEG) both in the plane view and ion milled cross section investigations (see below). The instrument was equipped with Oxford Inca energy dispersive X-ray detector (EDX) system. Chemical composition analysis was performed with an Oxford Inca energy dispersive X-ray system (EDX). Imaging was performed using a range of acceleration voltages, 5–20 kV. SEM/EDX was used for local chemical analysis as well as elemental mapping of the corroded metal surfaces and the ion milled cross sections.

2.4.4. Focused ion beam milling (FIB) and broad ion beam milling (BIB)

The distribution of elements after exposures was studied on the cross sections of samples prepared by broad ion beam milling (BIB) and focused ion beam milling (FIB) methods using a Leica EM TIC 3X ion beam slope cutter and an FEI Versa 3D system, respectively. The BIB cross sectioning is a relatively advanced technique that can be used to produce accurate cross sections with limited artifacts and distortion through the corrosion product and metal substrate in order to study the fragile corrosion layers.

Considering the larger surface area (around 1.5 mm in width and several hundred microns deep) of the cross sections produced by BIB in comparison with those of the FIB, the method was well-suited to study the corrosion pits on the heavily corroded samples. In the case of the BIB the sample holder was continuously cooled using liquid nitrogen in order to avoid any compositional change in the corrosion products. An argon ion beam with an acceleration voltage of 3 kV was chosen for the milling process. The cross sections were mainly made by BIB, but in the case of samples with very low amount of corrosion products, when precise positioning of the cross section was required, the FIB technique was used. The instrument is a dual beam system, equipped with both an electron and ion column. The electron column is equipped with a field emission gun (FEG) and the ion column with a liquid gallium source. Before milling, a 2 μm nickel layer was deposited by physical vapor deposition (PVD) onto the corroded samples, in order to protect the surface oxide from ion-induced damage.

3. Results

3.1. Gravimetric measurements

The dry mass gains as a function of exposure time for both materials are presented in Figs. 2 and 3 and Tables 2 and 3. The mass gain and metal loss data for the reference samples (exposed in the absence of salt) was in most cases negligible (<1 μm/year) and are not shown. All the gravimetric data, including the mass gain and metal loss values, are provided to enable quantitative comparisons of the influence of the different environmental factors on the atmospheric corrosion of the alloy AM50. Mass gain is a convenient way to measure average corrosion attack if the corrosion product composition is known. Also, mass gains can be used to compare corrosion rates if the corrosion products have similar composition. The tables also show the average metal loss of the

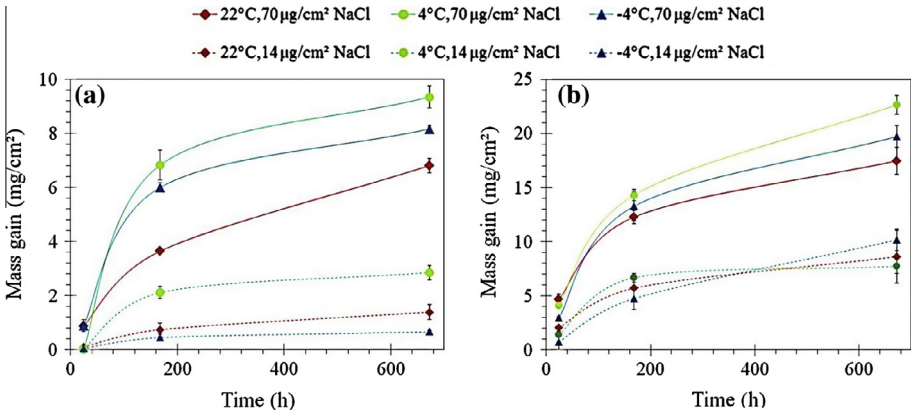

Fig. 2. The effect of temperature and exposure time on mass gain of 99.97% Mg: (a) 400 ppm CO_2. (b) CO_2-free. The standard errors for the data in Fig. 2a and b is less than 5 and 10%, respectively.

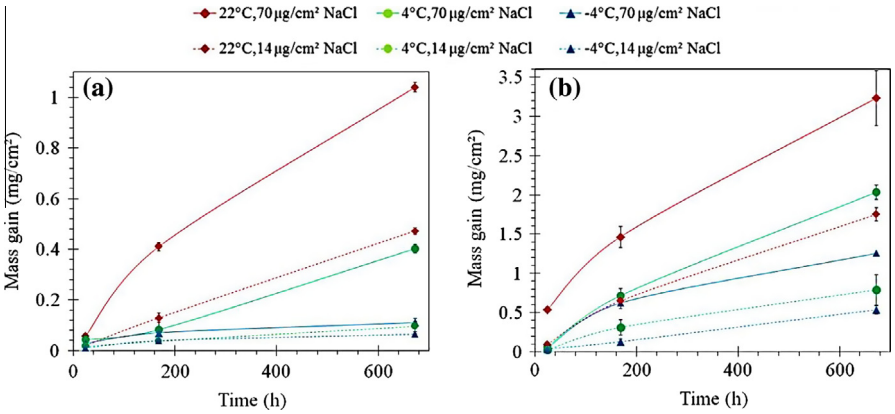

Fig. 3. The effect of temperature and exposure time on the mass gain of AM50: (a) 400 ppm CO_2. (b) CO_2-free. The standard errors for the data in Fig. 3a and b is less than 3 and 10%, respectively.

corroded samples. The ratio between the mass of the corrosion products and the metal loss for individual samples is also given. This value reflects the average corrosion product composition and can be compared to the corresponding ratios of selected corrosion products listed in Table 4. When the mass gain was <0.05 mg cm^{-2} metal loss could not be determined with sufficient precision and metal loss was calculated from the mass gain values, using the appropriate ratios of corrosion products identified by XRD (Table 4).

3.1.1. The effect of NaCl and exposure time

In the absence of NaCl, corrosion rates were very small, the mass gains registered after 4 weeks corresponding to an average corrosion rate of AM50 of <1 μm/year. The mass gains of unalloyed Mg are somewhat higher and the largest mass gain in the absence of salt was registered for 99.97% Mg after 672 h at 22 °C, in the absence of CO_2. As expected, the mass gains were much greater in the presence of salt, reflecting the corrosivity of NaCl towards Mg and Mg alloys under humid conditions. Figs. 2 and 3 show that most mass gain curves are convex, corresponding to a gradual slowing of the corrosion process. However, in the case of AM50 in the absence of CO_2 at −4 °C, the mass gain curve was linear.

3.1.2. Comparing 99.97% Mg and AM50

The mass gains of 99.97% Mg were considerably larger than those of the alloy, independent of the amount of salt, temperature and exposure time (Figs. 2 and 3). Also, the mass gain values of alloy AM50, relative to 99.97% Mg, increased with decreasing the temperature. For example, in the absence of CO_2 with 70 μg cm^{-2} salt, the mass gains of 99.97% Mg after 672 h were 6 times larger than those of AM50 at 22 °C while the corresponding factor was 16 at −4 °C. In the presence of CO_2, the corresponding factors were 7 at 22 °C and 50 at −4 °C. The metal loss data showed the same trends (see Tables 2 and 3).

3.1.3. The effect of CO_2

According to a previous study by this group [29], CO_2 inhibits the NaCl-induced atmospheric corrosion of 99.97% Mg and AM50 at 22 °C. The present results illustrate the strong inhibitive effect of CO_2 towards both pure Mg and the alloy at all three temperatures; see Fig. 4a and b. At 4 and −4 °C, the metal loss values of 99.97% Mg in the absence of CO_2 were 2–20 times greater than in the presence of 400 ppm CO_2 (Table 2). The corrosion inhibitive effect of CO_2 was even stronger for the alloy. The metal loss values of AM50 in the absence of CO_2 were greater by a factor of 9–20 (4 °C) and 6–14 (−4 °C) than in the presence of 400 ppm of CO_2 (Table 3). It should be noted that metal loss data should be used rather than mass gain data when investigating the corrosion inhibitive effect of CO_2 as the corrosion product composition is strongly influenced by CO_2.

3.1.4. The effect of temperature

In order to illustrate the influence of temperature on atmospheric corrosion behavior of the investigated alloys, the dry mass gain and metal loss values after 168 h as function of exposure temperatures are plotted in Fig. 4. The corresponding data for the cases

Table 2
Metal losses, corrosion rates and experimental corrosion product ratios for 99.97% Mg.

CO_2	Temperature	NaCl (μg/cm^2)	Exposure time (h)	Metal loss (mg/cm^2)	Ratio (X)[a]	Corrosion rate (μm/year)
400 ppm	22	14	24	0.08 ± 0.02	2.1	
400 ppm	22	14	168	0.32 ± 0.04	3.3	
400 ppm	22	14	672	0.50 ± 0.02	3.8	52 ± 1
400 ppm	4	14	24	0.04 ± 0.01	4.0	
400 ppm	4	14	168	1.11 ± 0.21	2.9	
400 ppm	4	14	672	0.58 ± 0.12	2.4	64 ± 4.2
400 ppm	−4	14	24	0.12 ± 0.06	1.3	
400 ppm	−4	14	168	0.29 ± 0.09	2.5	
400 ppm	−4	14	672	0.37 ± 0.08	2.8	27 ± 3
400 ppm	22	70	24	0.41 ± 0.02	2.8	
400 ppm	22	70	168	1.99 ± 0.14	2.8	
400 ppm	22	70	672	3.37 ± 0.32	3.0	239 ± 21
400 ppm	4	70	24	0.01 ± 0.005	2.0	
400 ppm	4	70	168	3.83 ± 0.34	2.8	
400 ppm	4	70	672	5.18 ± 0.83	2.8	355 ± 46
400 ppm	−4	70	24	0.51 ± 0.05	2.7	
400 ppm	−4	70	168	3.15 ± 0.31	2.9	
400 ppm	−4	70	672	2.68 ± 0.43	2.9	199 ± 28
0	22	14	24	1.40 ± 0.23	2.5	
0	22	14	168	3.40 ± 0.29	2.7	
0	22	14	672	5.70 ± 0.48	2.5	546 ± 27
0	4	14	24	0.89 ± 0.21	2.5	
0	4	14	168	2.27 ± 0.33	2.5	
0	4	14	672	4.30 ± 0.54	2.7	294 ± 32
0	−4	14	24	0.55 ± 0.08	2.3	
0	−4	14	168	3.33 ± 0.19	2.4	
0	−4	14	672	7.53 ± 0.95	2.3	601 ± 49
0	22	70	24	3.45 ± 0.84	2.3	
0	22	70	168	7.03 ± 1.22	2.7	
0	22	70	672	15.50 ± 2.34	3.6	1161 ± 64
0	4	70	24	2.61 ± 0.24	2.6	
0	4	70	168	6.91 ± 1.12	3.1	
0	4	70	672	12.41 ± 1.45	2.8	773 ± 58
0	−4	70	24	2.14 ± 0.44	2.4	
0	−4	70	168	7.26 ± 1.2	2.8	
0	−4	70	672	12.74 ± 2.23	2.5	993 ± 49

[a] Ratio of the dominant corrosion product detected by XRD.

of 24 and 672 h are listed in Tables 2 and 3. The mass gain and metal loss results after 168 h show that the effect of temperature on the rate of NaCl-induced corrosion of 99.97% Mg was different from the case of alloy AM50, see Fig. 4. For the alloy, increasing the temperature from −4 °C to 22 °C significantly increased the average rate of corrosion, irrespective of the amount of added NaCl and both in the absence and in the presence of CO_2, as shown in Fig. 2. The effect of temperature on alloy AM50 was especially marked in the presence of CO_2. Hence, between −4 and 22 °C, the rate of NaCl-induced corrosion of AM50 increased by a factor of about 6 and 4.5 in the presence and absence of CO_2, respectively (Table 3 and Fig. 4b). In the case of 99.97% Mg, there was a negative correlation between corrosion rate and temperature in the presence of CO_2, corrosion was significantly slower at 22 °C compared to 4 and −4 °C (Fig. 4a). In contrast, the effect of temperature was not significant in the absence of CO_2.

3.2. Corrosion product composition

The phases identified by XRD on samples and also the ratios between formula mass and the mass of the metal ions for the corrosion products are presented in Table 4. The crystalline phases identified after exposures at three temperatures are shown in Table 5. The crystalline corrosion products at 4 and 22 °C were the same. In the absence of both NaCl and CO_2, traces of brucite were identified on 99.97% Mg but not on AM50. In the absence of salt and in the presence of CO_2, no crystalline products were found. NaCl-induced corrosion in the absence of CO_2 resulted in the formation of brucite on both materials. In the case of the alloy, the magnesium aluminum hydroxide meixnerite ($Mg_6Al_2(OH)_{18} \times 4.5H_2O$) was also identified. In the presence of CO_2 and NaCl, both materials produced three magnesium hydroxy carbonates; H4, H5 and H8 (Table 4). In some cases, the diffractograms contained additional weak peaks that could not be attributed to a known compound.

The corrosion products identified after exposure at −4 °C were different from those formed at higher temperatures. Therefore, the only crystalline compounds identified at −4 °C were brucite (on 99.97%Mg and AM50) and meixnerite (on AM50) after exposure with NaCl in the absence of CO_2 (Table 5). Interestingly, the crystalline hydroxy carbonates formed under these conditions at 4 and 22 °C were absent at −4 °C. Instead an unknown phase appeared (U1 in Table 5) in most cases, with reflections at d = 4.58 Å and d = 2.95 Å. The unknown phase is illustrated by Fig. 5a and b, showing diffractograms acquired from 99.97% Mg and AM50 exposed in the absence of CO_2 at −4 °C. FTIR spectra acquired from samples exposed after 672 h exposure at −4 °C and 4 °C are depicted in Fig. 5d. The absorption bands at 1435, 1488 cm^{-1} on the sample exposed at 4 °C correspond to carbonate, in accordance with the identification of magnesium hydroxy carbonate by XRD analysis (Table 5).

3.3. Microscopy of corrosion of alloy AM50

The microstructure of alloy AM50 investigated is described elsewhere [18,42]. The main microstructural constituents are shown in the plan-view SEM image and cross section image in Fig. 10a and b. The alloy is composed of α-Mg grains and a partially

Table 3
Metal losses, corrosion rates and experimental corrosion product ratios for the alloy AM50.

CO_2	Temperature	NaCl (μg/cm^2)	Exposure time (h)	Metal loss (mg/cm^2)	Ratio (X)	Corrosion rate (μm/year)
400 ppm	22	14	24	0.01[b]	4.0	
400 ppm	22	14	168	0.04 ± 0.001	4.2	
400 ppm	22	14	672	0.15 ± 0.02	4.1	11 ± 1
400 ppm	4	14	24	0.01[b]	4.0	
400 ppm	4	14	168	0.01[b]	4.0	
400 ppm	4	14	672	0.03 ± 0.01	4.0	2 ± 1
400 ppm	−4	14	24	<0.01[b]	[a]4.0	
400 ppm	−4	14	168	0.01[b]	4.0	
400 ppm	−4	14	672	0.04 ± 0.001	2.5	3 ± 1
400 ppm	22	70	24	0.03 ± 0.001	4.0	
400 ppm	22	70	168	0.13 ± 0.003	4.2	
400 ppm	22	70	672	0.34 ± 0.002	4.1	25 ± 1
400 ppm	4	70	24	0.01[b]	4.0	
400 ppm	4	70	168	0.02[b]	5	
400 ppm	4	70	672	0.13 ± 0.006	4.1	10 ± 1
400 ppm	−4	70	24	0.01[b]	2.5	
400 ppm	−4	70	168	0.03 ± 0.001	3.3	
400 ppm	−4	70	672	0.05 ± 0.001	3.2	4 ± 1
0	22	14	24	0.12 ± 0.003	1.7	
0	22	14	168	0.15 ± 0.002	2.7	
0	22	14	672	1.08 ± 0.14	2.6	78 ± 4.5
0	4	14	24	0.04 ± 0.001	[a]2.4	
0	4	14	168	0.20 ± 0.05	2.5	
0	4	14	672	0.46 ± 0.12	2.7	45 ± 4.2
0	−4	14	24	<0.01[b]	[a]2.4	
0	−4	14	168	0.10 ± 0.002	2.3	
0	−4	14	672	0.34 ± 0.09	2.6	26 ± 1
0	22	70	24	0.36 ± 0.07	2.5	
0	22	70	168	0.90 ± 0.12	2.6	
0	22	70	672	2.10 ± 0.19	2.5	124 ± 5.2
0	4	70	24	0.03 ± 0.001	3.0	
0	4	70	168	0.43 ± 0.04	2.6	
0	4	70	672	1.23 ± 0.13	2.9	89 ± 4.4
0	−4	70	24	0.01[b]	2.3	
0	−4	70	168	0.20 ± 0.002	2.6	
0	−4	70	672	0.72 ± 0.11	2.7	53 ± 4.2

[a] Ratio of the dominant corrosion product detected by XRD.
[b] The scatter for these cases were negligible (<±0.001 mg/cm^2).

Table 4
Crystalline phases identified by XRD. Two corrosion products are included (in italics) that were not positively identified but are considered possible candidates.

Name	Formula	Abbreviation	Corrosion product ratio (total mass/mass of metal ions)
Magnesium	α-Mg	Mg	–
β-phase	$Mg_{17}Al_{12}$	β	–
Brucite	$Mg(OH)_2$	B	2.40
Hydromagnesite (1)	$Mg_5(CO_3)_4(OH)_2 \times 4H_2O$	H4	3.85
	$Mg_5(CO_3)_4(OH)_2 \times 5H_2O$	H5	4.00
Giorgiosite	$Mg_5(CO_3)_4(OH)_2 \times 8H_2O$	H8	4.44
Meixnerite	$Mg_6Al_2(OH)_{18} \times 4.5H_2O$	Meix	4.02
Hydrotalcite	$Mg_6Al_2(OH)_{16}CO_3 \times 4H_2O$		*4.20*
	$Mg_2Cl_2CO_3 \times 7H_2O$		*4.82*

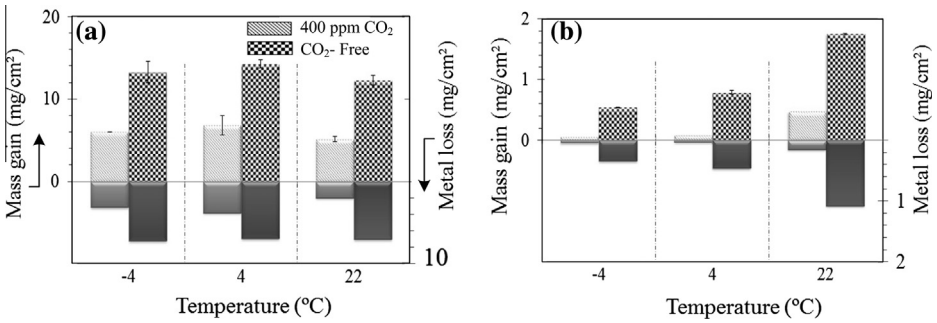

Fig. 4. The effect of temperature on the mass gain and metal loss (70 μg cm^{-2} NaCl, 168 h) (a) 99.97% Mg, (b) AM50.

Table 5
Phases identified by XRD after exposure at the three temperature. Abbreviations are explained in Table 4. The presence of an unidentified crystalline corrosion product is indicated by the letter U and U1.

Material	CO_2 (ppm)	NaCl (μg/cm^2)	Exposure time (h)	Crystalline phases detected		
				From base alloy	4 and 22 °C	−4 °C
AM50	400	0	All	Mg(s), β (w)		U1 (after 672 h)
AM50	400 ppm	70	24	Mg(s), β (w), NaCl(s)		
AM50	400 ppm	70	672	Mg(s), NaCl	H8, H5, H4, U	U1
AM50	0	0	All	Mg(s), β (w)		U1 (after 672 h)
AM50	0	70	24	Mg(s), NaCl	B, Meix	B
AM50	0	70	672	Mg(s)	B, Meix	B, Meix, U1
Mg	400 ppm	0	All	Mg(s)		
Mg	400 ppm	70	24	Mg(s), NaCl	B	U
Mg	400 ppm	70	672	Mg(s)	B, H5, H4, H8	B
Mg	0	0	24	Mg(s)		B, U1
Mg	0	0	672	Mg(s)	B	B, U1
Mg	0	70	24	Mg(w)	B	U1
Mg	0	70	672	Mg(w)	B	B, U1

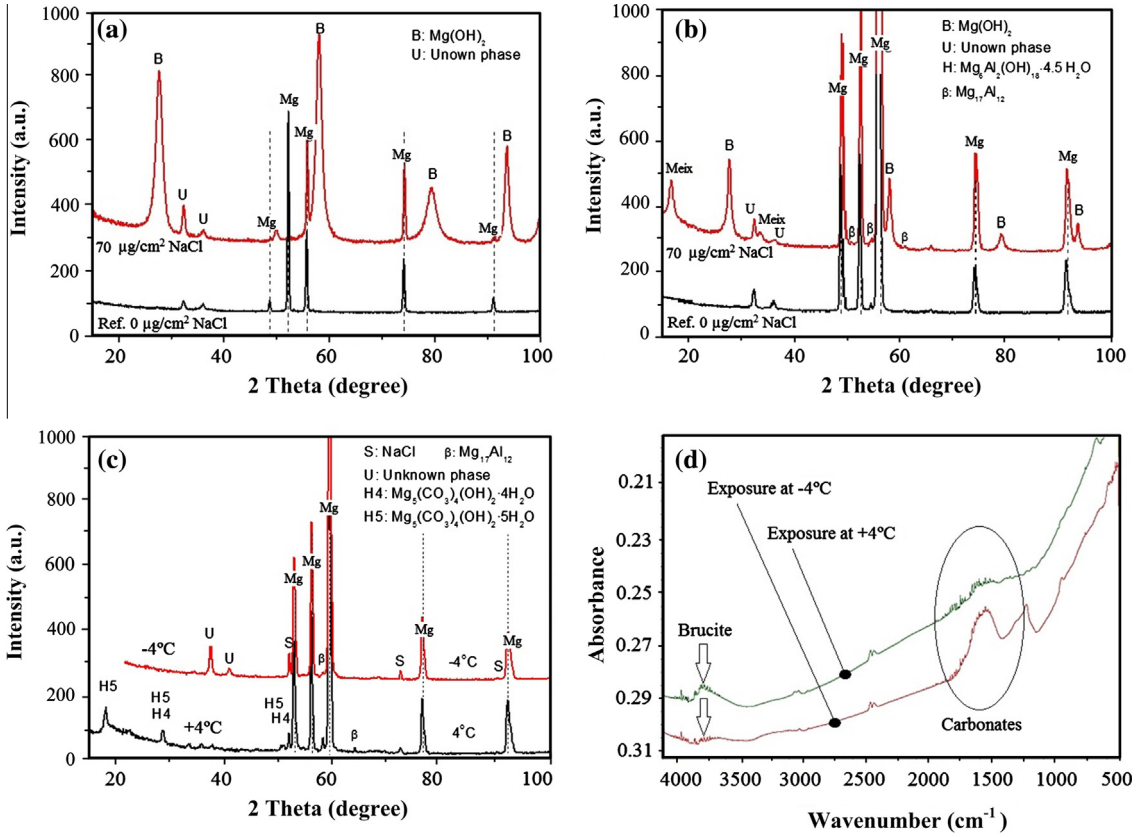

Fig. 5. XRD patterns of (a) 99.97% Mg and (b) AM50 exposed for 672 h at −4 °C in the absence of CO_2 and NaCl (lower (black) pattern) and in the presence of 70 μg/cm^2 NaCl (upper (red) patterns). (c) XRD patterns of AM50 exposed for 672 h at −4 °C and 4 °C in the presence of CO_2 with 70 μg/cm^2 NaCl. (d) two representative FTIR spectra of AM50 after 672 h at −4 and 4 °C in the presence of CO_2 and with 70 μg/cm^2 NaCl. (For interpretation of the references to colour in this figure legend, the reader is referred to the web version of this article.)

divorced α + β eutectic. In addition, η phase ($Al_8Mn_5(Fe)$) particles are present, usually in the α + β eutectic region. The plan-view SEM images in Figs. 6–9 show the morphology of the corroded metal surface after exposure. It may be noted that in the present study all corrosion products, including the water soluble ones, remain on the metal surface during the exposures, which is not the case in *e.g.*, immersion testing [15,16].

The strongly corrosive nature of NaCl is illustrated in Fig. 6. As seen, there is little evidence of corrosion in the absence of salt and the extent of corrosion increases with the amount of salt added. This is in accord with the gravimetric results (Tables 2 and 3). The sample that had corroded in the presence of 70 μg cm^{-2} of salt in the presence of CO_2 exhibits unreacted NaCl after 672 h exposure, which could also be identified by XRD (Table 5). Fig. 7 illustrates the effect of exposure time on corrosion morphology for NaCl contaminated AM50 exposed in the absence of CO_2 at 4 °C. As expected, there was a considerable increase in the extent of corrosion from 24 to 672 h (Fig. 7a and b). After 24 h, corrosion product agglomerations had formed on the surface (grey and dark grey) and large amounts of unreacted NaCl were present. The NaCl crystallites correspond to a NaCl (aq) solution that was present at the end of the exposure and that has crystallized upon drying. After

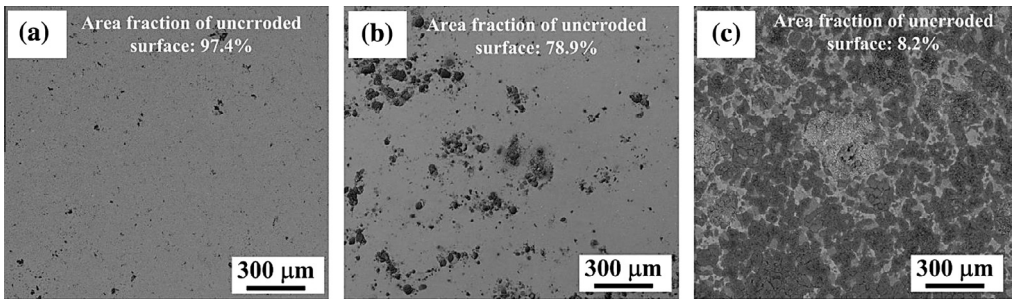

Fig. 6. The effect of NaCl on corrosion morphology on alloy AM50, 4 °C, 672 h, 400 ppm CO_2 (a) no NaCl, (b) 14 μg/cm^2 NaCl, (c) 70 μg/cm^2 NaCl.

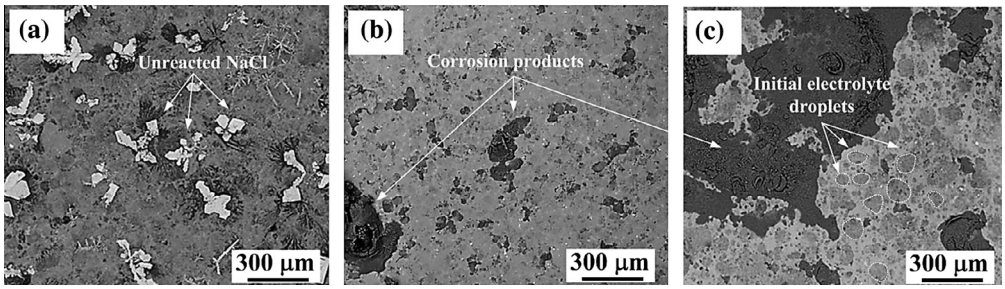

Fig. 7. The effect of time on corrosion morphology on alloy AM50, 4 °C, 70 μg/cm^2 NaCl, CO_2-free (a) 24 h, (b) 168 h and (c) 672 h.

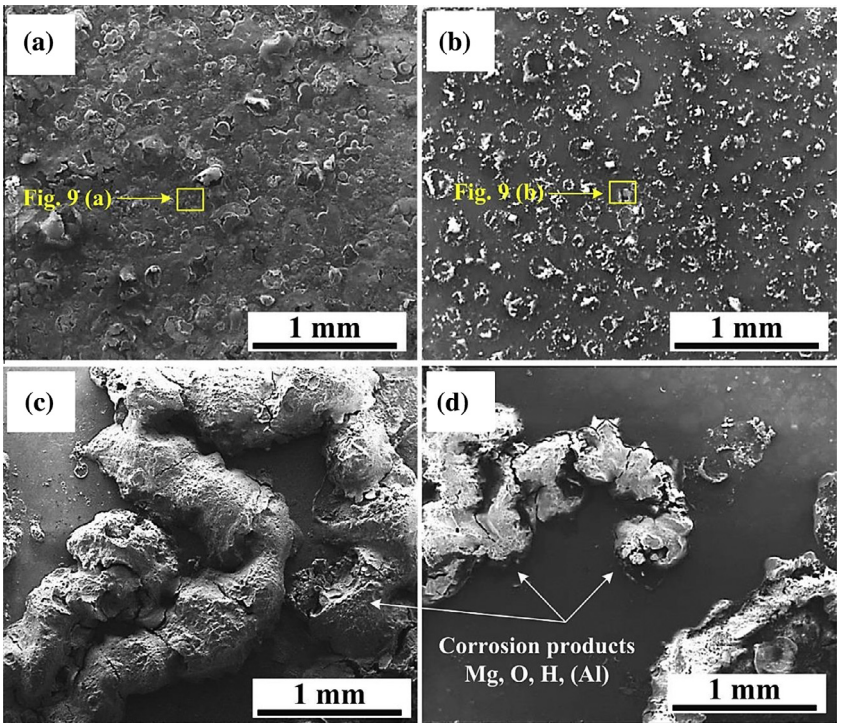

Fig. 8. SEM secondary electron images showing the effect of temperature on the corrosion morphology of alloy AM50, 70 μg/cm^2 NaCl, 672 h (a) 22 °C, 400 ppm CO_2, (b) −4 °C 400 ppm CO_2, (c) 22 °C, CO_2-free and (d) −4 °C, CO_2-free.

672 h, NaCl was no longer detected on the surface that was also in accordance with the XRD analysis (Table 5). The roughly circular surface features (as shown in Fig. 7c) of about 20–100 μm diameter correspond to electrolyte droplets that formed at the start of the exposure.

The effect of exposure temperature on the morphology of the corroded surface in the presence and absence of CO_2 at −4 and 22 °C is illustrated in Fig. 8. The corresponding exposures at 4 °C are shown in Fig. 6c and Fig. 7c. In accordance with the gravimetric results in Tables 2 and 3, there was a strong positive correlation between the extent of corrosion and temperature, both in the absence and in the presence of CO_2. The corrosion inhibitive effect of CO_2 was also evident from the images (compare Fig. 8a, b with c, d (−4 and 22 °C) and Figs. 6 and 7 (4 °C). Thus, the samples least affected by corrosion are the ones exposed at −4 °C in the presence of CO_2 (Fig. 8b), the image revealing circular corrosion product

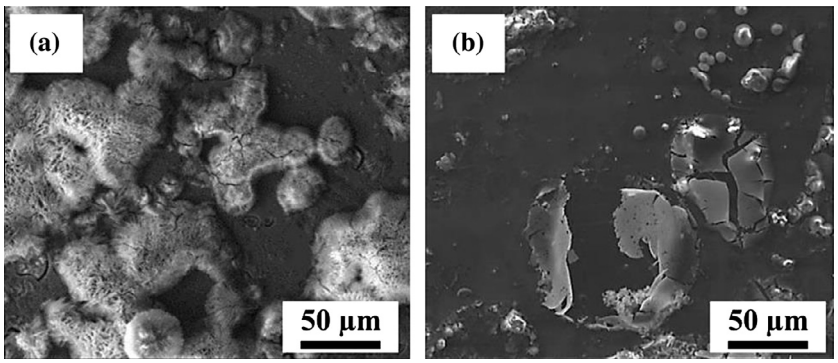

Fig. 9. SEM secondary electron images showing the corrosion product morphology after 672 h exposure with 70 µg/cm^2 NaCl in the presence of CO_2; (a) at 22 °C, (b) at −4 °C.

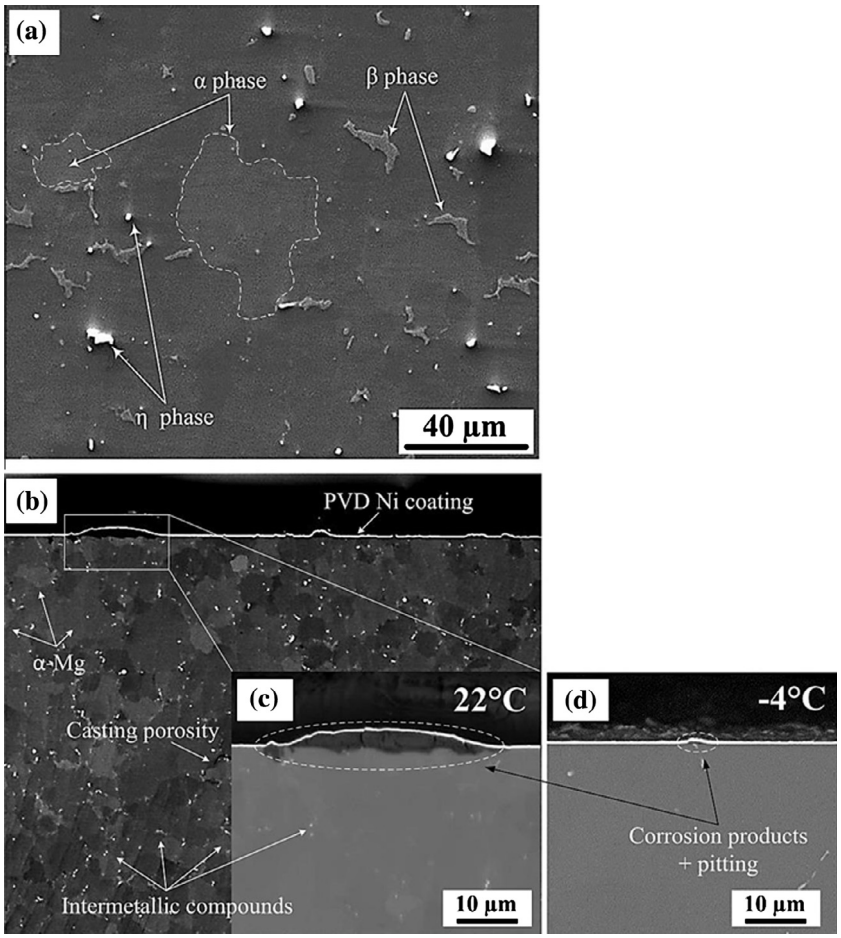

Fig. 10. SEM images of (a) metal surface showing the as-cast microstructure of the alloy AM50. (b–d) SEM secondary and backscattered electron images of BIB-prepared cross-sections and plane view image of alloy AM50 exposed in the presence of CO_2 and 14 µg/cm^2 NaCl after 168 h at 22 and −4 °C. Nickel was deposited on the top surface to protect the corrosion product. The difference in brightness between different α-Mg grains is the result of channeling contrast.

accumulations on an otherwise smooth surface. The corresponding exposure at 22 °C resulted in a much more strongly corroded surface with corrosion product crusts covering most of the surface. The circular features correspond to NaCl (aq) droplets that formed when the samples were introduced into the humid exposure environment. It may be noted that the morphology is rather different from that described for corrosion products on Mg Al alloys exposed in the outdoor atmosphere [23,24]. This is because the latter have been subjected to repeated wet-dry cycling, resulting in the formation of cracks and crack rings around the corrosion crusts.

The strong effect of temperature in the presence of CO_2 is in agreement with the gravimetric results. Exposures in the absence of CO_2 resulted in a very different corrosion morphology, see Fig. 8c and d. Thus, extensive worm-like corrosion products appeared at all three temperatures, the area between the corrosion product accumulations was being relatively unaffected by corrosion. As expected, the most severe corrosion was observed at 22 °C in the absence of CO_2 while the exposure at −4 °C in the presence of 400 ppm CO_2 represented the mildest corrosive conditions. CO_2 had a similar effect on corrosion morphology at all three

temperatures, producing a much more uniform corrosion attack compared to the samples exposed in the absence of CO_2.

The corrosion morphology observed in the presence of CO_2 at 4 °C and 22 °C is dominated by plate-like clusters, the plates were being oriented perpendicular to the sample surface (Fig. 9). These corrosion product aggregates were highly porous. Similar corrosion product morphologies have also been reported previously for Mg alloys [35,43,44] and are suggested to correspond to the magnesium hydroxy carbonates.

The samples exposed at −4 °C exhibited a completely different morphology; the corrosion products were being dominated by egg-shell like features, see Fig. 9. It may be noted that the absence of the needle-like corrosion products at −4 °C was accompanied by a lack of evidence for crystalline magnesium hydroxy carbonates by XRD. Compared to the NaCl-induced corrosion of alloy AM50 at 22 °C and 400 ppm CO_2, the corresponding exposure at −4 °C resulted in very few corrosion crusts owing to the slow corrosion rate (see SEM image of BIB-prepared cross section in Fig. 10).

Because of the severe corrosion attack at 22 °C it was possible to find corrosion pits in the BIB-prepared cross sections (Fig. 10d). However, this was not possible at −4 °C because of the mild corrosion attack. To locally investigate the corrosion attack at −4 °C, FIB-prepared cross-sections were used instead. Fig. 11 shows the SEM backscattered electron image and EDX maps of the cross section for Al, C, O, Cl and Mn acquired after 168 h exposure in the presence of CO_2. The image shows a corrosion product of varying thickness and pits in the alloy. The elemental mapping shows that Cl is concentrated in the bottom of the pits. Also, the pits are situated in the vicinity of areas where β phase is present (see Al map in Fig. 11). An η-phase particle can be seen in the backscattered image and in the Mn map. Al is scarce in the corrosion product which is dominated by Mg. The carbon map shows that the chlorine-rich areas are also rich in carbonate. The sodium signal was not significant because of low concentration and to overlap with magnesium in the EDX spectrum.

As noted above, the corrosion of alloy AM50 is more severe and localized in the absence of CO_2 at all temperatures. Fig. 12 shows the top-view of the AM50 alloy after 168 h exposure at −4 °C in the absence of CO_2. The image may be compared to the Fig. 8d, where corrosion is more pronounced both because of longer exposure time (672 h) and higher salt concentration (70 μg/cm^2). Fig. 12 shows a secondary electron image and a close-up of a relatively uncorroded part of the surface, at a distance from the localized attack. The quantitative elemental analysis of the partly detached corrosion product layer indicates that it is enriched in sodium and poor in chlorine. The elemental analysis indicates that relatively high amounts of carbonate are present. It is suggested that the carbonate has formed during sample handling and that the sodium-rich areas originally consisted of NaOH. The relatively low concentration of Al indicates that meixnerite ($Mg_6Al_2(OH)_{18} \times 4.5H_2O$) is absent in this area.

4. Discussion

The gravimetric results (Tables 2 and 3, Figs. 3 and 4) and the corrosion morphology (Figs. 6–9) illustrate the well-known corrosiveness of NaCl towards Mg and Mg alloys [10,11], the rate of atmospheric corrosion being very low (<1 μm/year) in the absence of salt. The NaCl added before exposure forms an aqueous solution in the experimental conditions (95% RH) at all three temperatures investigated. Accordingly, droplets consisting of NaCl (aq) solution were observed on the surface in the beginning of the exposures. In many cases, circular features corresponding to these droplets are detected after exposure, see *e.g.*, Fig. 7d. Therefore, the NaCl-induced atmospheric corrosion processes investigated in this work occur in the presence of small amounts of aqueous solution.

According to [45,46] the equilibrium composition of the solution in the experimental conditions is 8.0% NaCl by weight. The corresponding solution does not form ice at −4 °C [47]. Mg–Al alloys are protected by a partially protective surface film that is dominated by brucite, $Mg(OH)_2$ [18,19]. According to Godard et al. [1] and Song et al. [11], Mg–Al alloys immersed in NaCl solution corrode by an electrochemical process where the anodic dissolution of magnesium occurs according to Eq. (4), and the cathodic reduction of water occurs at different sites (Eq. (5)). Accordingly, the dominant corrosion product is reported to be brucite, $Mg(OH)_2$, based on Eq. (6);

$$Mg(s) \rightarrow Mg^{2+}(aq) + 2e^- \quad (4)$$

$$2H_2O + 2e^- \rightarrow H_2(g) + 2OH^-(aq) \quad (5)$$

$$Mg^{2+}(aq) + 2OH^-(aq) \rightarrow Mg(OH)_2(s) \quad (6)$$

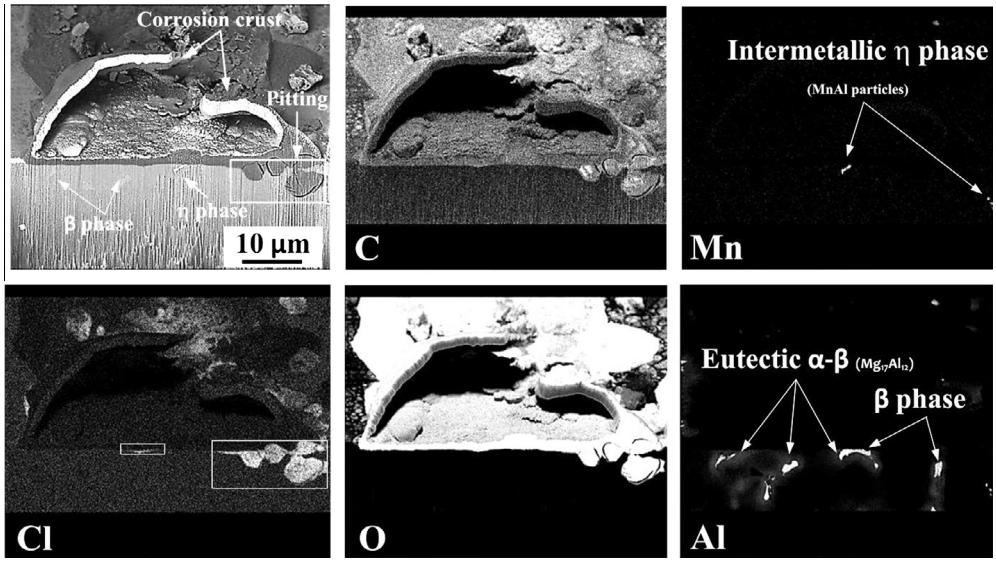

Fig. 11. SEM backscattered electron image and EDX maps of FIB-prepared cross-sections of alloy AM50 after 168 h exposure in the presence of 400 ppm CO_2 and 14 μg/cm^2 NaCl at −4 °C. The rectangles are showing the pitting corrosion and accumulations of Cl^- ions.

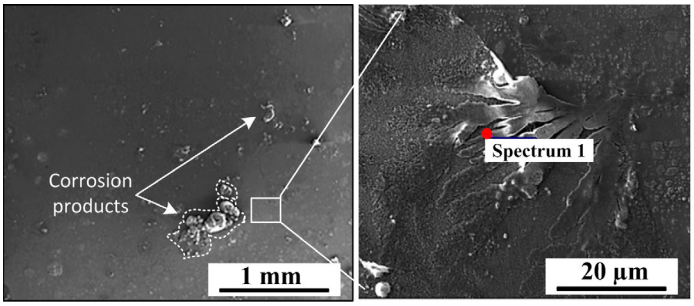

Spectrum 1

Element	Weight%
O	34.25
Na	27.91
Mg	25.24
C	9.63
Al	1.61
Cl	0.83
Si	0.53
Total	100

Fig. 12. The EDX analysis shows that sodium is enriched on the surface of the sample and the chlorine level is below the detection limit. Alloy AM50 exposed in the absence of CO_2 and 14 µg/cm^2 NaCl after 168 h at −4 °C.

Electrochemical corrosion in a NaCl (aq) solution is expected to result in the accumulation of $MgCl_2$ (aq) at the anodic sites and of NaOH (aq) at the cathodic sites. Because $Mg(OH)_2$ is insoluble at high pH, the film is stabilized in the cathodic areas. In contrast, the anodic dissolution of Mg in neutral solution is reported to be enhanced by Cl^- (aq) [48]. Hence, Mg corrosion is expected to be strongly localized in the presence of NaCl (aq). Brucite is an electronic insulator and therefore a poor electrode for the cathodic process. Hence, the corrosion of Mg is greatly accelerated by cathodically active, intermetallic precipitates containing, *e.g.*, Fe [18]. Therefore, commercial Mg alloys are alloyed with Mn to decrease the detrimental effects of traces of Fe in the alloy [18,19]. In the presence of Mn, Fe tends to dissolve in the Al_8Mn_5 (η-phase), which is not very active as a cathode. The observation that the NaCl-induced atmospheric corrosion of alloy AM50 is slower than for 99.97% Mg can be partially attributed to the beneficial effect of Mn alloying. According to Jönsson et al. [33] who investigated the atmospheric corrosion of commercial Mg–Al alloys, micro-galvanic elements are established where the anodic dissolution mainly occurs in the middle of the primary α-dendrite grains and the cathodic process mainly occurs on the eutectic α/β constituent.

The present results are in accordance with an electrochemical nature of corrosion, as illustrated both by the tendency of corrosion to be localized and by the redistribution of sodium and chloride ions on the surface. Therefore, in CO_2-free conditions, part of the surface is covered by voluminous corrosion products while the rest is only slightly corroded (Fig. 7c and Fig. 8c and d). Also, the quantitative EDX analyses show that sodium is enriched on the uncorroded metal surface at a distance from the location of corrosion attack, indicating the presence of cathodic sites, see Fig. 12. The observation that sodium and chlorine accumulate at sites corresponding to cathodic and anodic sites, respectively, is in accordance with a recent study Song et al. [49], where Mg alloys were subjected to salt-spray and immersion exposures. In contrast, Liao et al. [24] reports that very little chlorine was detected in the corrosion pits formed on two AZ31B magnesium alloys exposed in outdoor urban atmospheric environments. It is suggested that the scarce evidence for chloride in the corrosion pits of field exposed Mg alloys is due to a relatively low exposure to chloride in combination with the leaching of the corrosion products by rain. In the present work, the availability of chloride is relatively high and there is no leaching effect at all. We should also keep in mind that the use of de-icing salt on the roads creates a corrosive environment in the wintertime that is far richer in chloride than test sites with typical urban or industrial atmospheric conditions.

In this study we calculated the stoichiometric ratio (corrosion product mass/metal loss) of the corrosion products from the gravimetric results (Tables 2 and 3) and compared them to the corresponding stoichiometric ratios (molecular mass/ metal ion mass) of the identified corrosion products (Table 4). When evaluating the ratios presented in Table 3, it is seen that the corrosion product ratios for 99.97% Mg in the presence of NaCl and in the absence of CO_2 are about 2.4, corresponding to the stoichiometric ratio of brucite. This is in accordance with the XRD analysis which shows brucite to be the only crystalline corrosion product in this environment (see Table 5). Table 3 shows that the corrosion product ratio for alloy AM50 in the absence of salt tends to be slightly higher than 2.4. This is connected to the formation of the magnesium aluminum hydroxide meixnerite in that case which has a relatively high corrosion product ratio. Tables 2 and 3 show significantly higher corrosion product ratios in the presence of CO_2 formed on both materials. This also agrees well with the XRD analysis that identified three different magnesium hydroxy carbonates with formulas of $Mg_5(CO_3)_4(OH)_2 \times 4H_2O$, $Mg_5(CO_3)_4(OH)_2 \times 5H_2O$ and $Mg_5(CO_3)_4(OH)_2 \times 8H_2O$ having corrosion product ratios of 3.85, 4.00 and 4.44 respectively. The lower corrosion product ratios registered for 99.97% Mg compared to AM50 in the presence of CO_2 are in accordance with the identification of brucite by XRD (Table 5).

Significantly, the average corrosion rate is much higher in the absence of CO_2 (Tables 2 and 3). The inhibitive effect of CO_2 on the NaCl-induced atmospheric corrosion of 99.97% Mg and alloy AM50 is a relatively well-known phenomenon [29,50].

CO_2 neutralizes the catholyte and causes precipitation of sparingly soluble, carbonate-containing corrosion products. The formation of these corrosion products is an indication of the active role of CO_2 in the atmospheric corrosion. When CO_2 dissolves in water, it forms carbonic acid (H_2CO_3 (aq)). In alkaline conditions carbonic acid forms carbonate according to the Eqs. (7) and (8). CO_2 also reacts with brucite, which is the primary corrosion product, and forms magnesium hydroxy carbonates, see *e.g.*, Eq. (9):

$$H_2CO_3(aq) + OH^-(aq) \rightarrow HCO_3^-(aq) \quad (7)$$

$$HCO_3^-(aq) + OH^-(aq) \rightarrow CO_3^{2-}(aq) \quad (8)$$

$$5Mg(OH)_2(s) + 4CO_2(aq) \rightarrow Mg_5(CO_3)_4(OH)_2 \cdot 4H_2O(s) \quad (9)$$

Accordingly, several crystalline magnesium hydroxy carbonates were identified after exposure at 4 and 22 °C. These products are non-conducting and cannot serve as cathodes. They are also less soluble than brucite at neutral pH [50] and may thus slow down corrosion by physically blocking the anodic sites. In the case of alloy AM50, CO_2 may also protect against corrosion by stabilizing the alumina component of the passive film which tends to dissolve at high pH [29]. The effect of CO_2 may be important for understanding the corrosion behavior of Mg alloys in cases where there is a limited supply of CO_2 *e.g.*, in crevices, lap joints and beneath coatings.

Corrosion attack is more evenly distributed in the presence of CO_2 (compare Fig. 8a, b with c, d). Thus, in the presence of

400 ppm CO_2, there are no extensive uncorroded regions, corrosion initially being confined to the NaCl (aq) droplets. In recent paper by Shahabi et al. [29] reporting on the effect of CO_2 on the atmospheric corrosion of Mg and MgAl alloys, it was suggested that in the absence of CO_2, a high pH develops in the NaCl (aq) droplet periphery which decreases surface tension at the electrolyte/oxide interface and causes spreading of the electrolyte and droplet coalescence so that large areas on the surface become electrochemically connected. It was argued that CO_2 counteracts this effect by neutralization, explaining the smaller corrosion cells in the presence of CO_2.

Fig. 13 visualizes the cross section of the alloy presented in Fig. 11. Here, attention is drawn to the anodic pits developed in the presence of CO_2 that tend to occur in the periphery of the NaCl (aq) droplets (as presented in Figs. 10 and 11) and to the magnesium containing corrosion product precipitates (magnesium hydroxy carbonate) that cover the surface of the former droplets. It is suggested that the presence of a solid precipitate on the surface of the droplet restricts the availability of CO_2 in the droplet interior. Under those circumstances one may expect high pH to develop on the cathodic areas (presumed to be mainly β-phase areas) in the center of the droplet where CO_2 availability is expected to be the least. This would stabilize the brucite-based film, and the anodic reaction would run preferentially where the CO_2 availability is greater, and pH lower, i.e., in the droplet periphery.

Fig. 13 visualizes the cross section of the alloy presented in Fig. 11. Here, attention is drawn to the anodic pits developed in the presence of CO_2 that tend to occur in the periphery of the NaCl (aq) droplets (as presented in Figs. 10 and 11) and that magnesium containing corrosion product precipitates (magnesium hydroxy carbonate) cover the surface of the former droplets. It is suggested that the presence of a solid precipitate on the surface of the droplet restricts the availability of CO_2 in the droplet interior. Under those circumstances one may expect high pH to develop on the cathodic areas (presumed to be mainly β-phase areas) in the center of the droplet where CO_2 availability is expected to be the least. This would stabilize the brucite-based film, and the anodic reaction would run preferentially where the CO_2 availability is greater, and pH lower, i.e., in the droplet periphery.

4.1. The effect of temperature

It is well-known that variations in temperature profoundly influence the rate of atmospheric corrosion. The effect is mainly due to concomitant changes in the relative humidity that affect the amount of water on the metal surface and thereby the availability of electrolyte. In order to investigate the temperature effect *per se*, all exposures in the present study are performed at the same relative humidity (=95%). Because NaCl absorbs water to form an aqueous solution at RH > 75% in the temperature range studied, this means that the samples are exposed to NaCl (aq) solution during the exposures. It may be noted that the composition of the NaCl (aq) electrolyte (a_w = 0.95) has a very weak dependence on temperature [51]. Therefore, the amount and composition of the NaCl (aq) solution is nearly the same at the three temperatures investigated (22, 4 and −4 °C). Hence, we can be confident that the changes in corrosion behavior that we observe as a function of temperature are due to temperature only and not to differences in the availability of aqueous electrolyte on the surface or to the composition of that electrolyte. Once the influence of temperature on atmospheric corrosion is known, it becomes meaningful and interesting to investigate how variations in the relative humidity affects corrosion at different temperatures. However, such a study is outside the scope of this paper.

The introduction mentions a few laboratory investigations of atmospheric corrosion below room temperature. It is notable that the reported correlations between corrosion rate and temperature (keeping the activity of water constant) are very different. A positive correlation between corrosion rate and temperature (AZ91/NaCl and Al/NaCl) suggests that there is a rate-determining step in the corrosion process which is thermally activated, showing an Arrhenius-type behavior. This kind of behavior is expected since the chemical and electrochemical reactions involved in the anodic and cathodic reactions are thermally activated. Also, the conductivity of the electrolyte is related to ionic diffusion which is thermally activated. The inverse correlation of corrosion rate with temperature that has been reported in some cases is more unexpected [38,52]. In the case of the Zn/air + SO_2 system the effect was attributed to the precipitation of zinc hydroxy sulfate, forming a protective layer and removing ions from the electrolyte. The precipitate reportedly only nucleated at room temperature. Thus, $ZnSO_4$ (aq) electrolyte coexisted with solid ZnO (s) on the metal surface at low temperature, explaining the faster corrosion. In the case of Pb/air + gaseous acetic acid, it was suggested that the rate of corrosion was limited by the adsorption of acetic acid molecules on the lead surface. The adsorption of a gas on a surface is exothermic and the equilibrium amount of adsorbed gas thus decreases with increasing temperature.

The present results show a strong positive temperature dependence for the NaCl-induced corrosion of alloy AM50, especially in the presence of CO_2 (see Fig. 4b, Fig. 8a and b, Table 3). In the case of 99.97% Mg the effect of temperature is more complex (see Fig. 4a, Table 2). Thus, there is no significant correlation between temperature and corrosion rate in the absence of CO_2 while the corrosion rate is at its maximum at 4 °C in the presence of

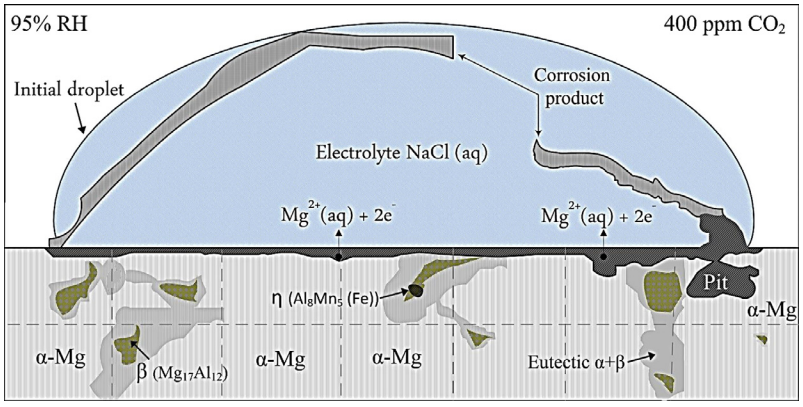

Fig. 13. Schematic illustration of the cross section of the alloy AM50 in the presence of CO_2 showing microstructural constituents and the formation of the pits (corresponds to the FIB-prepared cross section shown in Fig. 11).

400 ppm CO_2. It is suggested that the peculiar temperature dependence of the corrosion rate of 99.97% Mg in the presence of CO_2 is due to competing effects. Thus, the decreasing solubility of CO_2 in water with increasing temperature is expected to slow down carbonatization at higher temperature. Conversely, the hydration of CO_2 to form carbonic acid:

$$CO_2(aq) + H_2O \rightarrow H_2CO_3(aq) \quad (10)$$

This is a relatively slow, activated process that becomes faster at high temperature, promoting carbonatization. The absence of a clear temperature dependence of the corrosion of Mg and the strong positive temperature effect reported for NaCl-induced atmospheric corrosion of Al [37] suggests that the slowing of the rate of corrosion of alloy AM50 at 4 and −4 °C is related to the aluminum content in the alloy. Hence, the strong positive temperature dependence of the corrosion rate of alloy AM50 is suggested to be due to an activated process involving aluminum. One hypothesis is that the activated process consists of the dissolution of alumina in the film formed on the surface of the alloy.

It is observed that the inhibitive effect of CO_2 on the atmospheric corrosion becomes more pronounced at lower temperatures. At −4 °C the corrosion of alloy AM50 is ~13 times slower in the presence of CO_2 compared CO_2-free condition, while the corresponding factor is about 5 at 22 °C. This can be attributed to the fact that the solubility of CO_2 (as a corrosion inhibitor) in the aqueous electrolyte increases with decreasing temperature.

As expected, the corrosion product composition is strongly affected by CO_2. The XRD diffraction patterns acquired from alloy AM50 in the absence of CO_2 and in the presence of NaCl showed mainly brucite and traces of meixnerite ($Mg_6Al_2(OH)_{18} \times 4.5H_2O$), while the corresponding exposures in the presence of 400 ppm CO_2 at 4 and 22 °C resulted in the formation of magnesium hydroxy carbonates; giorgiosite, and two types of hydromagnesite, see Table 5 and Fig. 5a and b (the corrosion product composition at −4 °C is discussed below). The magnesium hydroxy carbonates may form either by reaction of brucite with gaseous CO_2 and H_2O or by precipitation from solution.

The prevalence of carbonate-containing corrosion products after exposure to 400 ppm CO_2 is similar to the behavior of Mg alloys exposed in the ambient atmosphere, where magnesium hydroxy carbonates (notably hydromagnesite) are usually dominant [23,24]. Sulfates have been reported to form in outdoor environments with high SO_2 concentration [25] while brucite has been reported to form in some cases of high corrosion rates in marine environments [53]. To our knowledge, meixnerite have not been reported as corrosion products previously. The suppression of meixnerite formation by CO_2 is explained by neutralization of the catholyte by CO_2 [38]. Thus, the alumina (AlOOH or $Al(OH)_3$) component in the film becomes soluble at high pH.

Surprisingly, temperature has a major effect on the corrosion product composition on both materials in the presence of CO_2. Thus, while several crystalline magnesium hydroxy carbonates were identified at 4 and 22 °C, the same compounds are absent at −4 °C. The large amount of corrosion products detected on 99.97% Mg in 400 ppm CO_2 at −4 °C (Table 5), shows that the lack of evidence for these compounds is not due to poor sensitivity of the XRD analysis. Also, the measurements were repeated several times. The analysis of the corrosion products by FTIR (Fig. 5d) indicates that the chemical composition of the corrosion product formed in the presence of CO_2 at −4 °C is similar to that formed in the presence of CO_2 at higher temperatures. Also, the corrosion product ratio is essentially the same at the different exposure temperatures (Table 3). Thus, it can be concluded that while magnesium hydroxy carbonates dominate in the presence of 400 ppm CO_2 regardless of temperature, they tend to be non-crystalline at −4 °C and crystalline at 4 and 22 °C. In addition to the non-crystalline products, there were weak diffraction lines from an unknown crystalline compound on 99.97% Mg in 400 ppm CO_2 (designated U in Table 5). It is possible that this compound contains carbonate. It is unlikely that the prevalence of non-crystalline corrosion products in 400 ppm CO_2 at −4 °C can explain the effect of temperature on the rate of atmospheric corrosion of alloy AM50. This is because 99.97% Mg, which does not show a strong effect of temperature on corrosion rate, also does not form the crystalline hydroxy carbonates detected at higher temperature under these conditions. In addition, the temperature effect on AM50 is also evident at 4 °C where the magnesium hydroxy carbonates are crystalline.

Yet another set of diffraction lines corresponding to an unknown phase were detected after exposure at −4 °C (designated U1 in Table 5). It is suggested that U1 may be a hitherto unknown low-temperature form of magnesium hydroxide. Additionally, from the obtained results it can be concluded that this phase does not contain Al, carbonate or chloride as U1 occurs both on AM50 and on 99.97% Mg and both in the presence and in the absence of CO_2 and NaCl. The task of identification and characterization of the unknown compounds U and U1 is outside the scope of this paper but will be the subject of further investigation.

5. Conclusions

Designing new exposure equipment enabled us to investigate the effect of temperature on the NaCl-induced atmospheric corrosion of 99.97% Mg and the Mg–Al alloy AM50. The effects of exposure time and CO_2 were studied at three temperatures, 22, 4 and −4 °C. The main conclusions drawn from this study are as follows:

- The NaCl-induced atmospheric corrosion of alloy AM50 shows a strong positive correlation with temperature. The effect of temperature was especially strong in the presence of CO_2. In contrast, 99.97% Mg did not exhibit a strong temperature dependence.
- 99.97% Mg and alloy AM50 corrode in humid air at −4 °C in the presence of NaCl because of the presence of an aqueous electrolyte.
- The temperature dependence of the corrosion of alloy AM50 is tentatively attributed to its aluminum content and the increased inhibitive effect of CO_2 at low temperature is suggested to be due to an increased solubility of CO_2 in the aqueous electrolyte at low temperature.
- In the absence of CO_2 the NaCl-induced atmospheric corrosion resulted in the same crystalline corrosion products at all three temperatures. Thus, brucite was formed on both materials. On alloy AM50, meixnerite ($Mg_6Al_2(OH)_{18} \times 4.5H_2O$) was also identified.
- NaCl-induced atmospheric corrosion in the presence of CO_2 resulted in the formation of three different magnesium hydroxy carbonates ($Mg_5(CO_3)_4(OH)_2 \times xH_2O$) at 22 and 4 °C. At −4 °C, however, NaCl-induced atmospheric corrosion resulted in the formation of a non-crystalline carbonate-containing corrosion product and an unknown crystalline compound.
- Anodic and cathodic sites were identified by EDX analyses on the FIB-prepared cross sections. Chloride mainly accumulates in the pits while sodium accumulate at a distance from the areas of corrosion attack, indicating the cathodic sites.
- For all exposure conditions the rate of atmospheric corrosion showed a positive correlation with the amount of NaCl added. The corrosion rates in the presence of CO_2 were significantly less than in the CO_2-free exposures for both materials, regardless of temperature.

Acknowledgment

The authors would like to express their thanks to The Swedish Foundation for Strategic Research (SSF) for funding this project.

References

[1] H.P. Godard, W.B. Jepson, M.R. Bothwell, R.L. Lane, The Corrosion of Light Metals, Wiley and Sons, New York, 1967.
[2] G.L. Markar, J. Kruger, Corrosion of magnesium, Int. Mater. Rev. 38 (1993) 138–153.
[3] K.U. Kainer, R.L. Edgar, Global Overview on Demand and Applications for Magnesium Alloy, Wiley-VCH Verlag GmbH, 2000.
[4] K.U. Kainer, F. Kaiser, Magnesium Alloys and Technology, Wiley-VCH GmbH, Weinheim, 2003.
[5] Z.M. Shi, G.L. Song, A. Atrens, Influence of anodising current on the corrosion resistance of anodised AZ91D magnesium alloy, Corros. Sci. 48 (2006) 1939–1959.
[6] A. Pardo, M.C. Merino, A.E. Coy, R. Arrabal, F. Viejo, E. Matykina, Corrosion behaviour of magnesium/aluminium alloys in 3.5 wt.% NaCl, Corros. Sci. 50 (2008) 823–834.
[7] M.M. Advedesian, H. Baker, Magnesium and Magnesium Alloys, ASM Specialty Handbook, ASM International, Materials Park, 1999.
[8] P.B. Srinivasan, C. Blawert, W. Dietzet, K.U. Kainer, Stress corrosion cracking behaviour of a surface-modified magnesium alloy, Scripta Mater. 59 (2008) 43–46.
[9] G.L. Makar, K. Kruger, Corrosion studies of rapidly solidified magnesium alloys, J. Electrochem. Soc. 137 (1990) 414–421.
[10] D.B. Blücher, J.E. Svensson, L.G. Johansson, The influence of CO_2, $AlCl_3{\cdot}6H_2O$, $MgCl_2{\cdot}6H_2O$, Na_2SO_4 and NaCl on the atmospheric corrosion of aluminum, Corros. Sci. 48 (2006) 1848–1866.
[11] G. Song, A. Atrens, M. Dargusch, Influence of microstructure on the corrosion of die-cast AZ91D, Corros. Sci. 41 (1999) 249–273.
[12] R. Tunold, H. Holtan, M.B. Berge, The corrosion of magnesium in aqueous solution containing chloride ions, Corros. Sci. 17 (1977) 353–365.
[13] M.C. Zhao, M. Liu, G. Song, A. Atrens, Influence of pH and chloride ion concentration on the corrosion of Mg alloy ZE41, Corros. Sci. 50 (2008) 3168–3178.
[14] G. Wu, Y. Fan, A. Atrens, C. Zhai, W. Ding, Electrochemical behavior of magnesium alloys AZ91D, AZCe2, and AZLa1 in chloride and sulfate solutions, J. Appl. Electrochem. 38 (2008) 251–257.
[15] F. Cao, Z. Shi, J. Hofstetter, P.J. Uggowitzer, G. Song, M. Liu, A. Atrens, Corrosion of ultra-high-purity Mg in 3.5% NaCl solution saturated with $Mg(OH)_2$, Corros. Sci. 75 (2013) 78–99.
[16] F. Cao, Z. Shi, G. Song, M. Liu, A. Atrens, Corrosion behaviour in salt spray and in 3.5% NaCl solution saturated with $Mg(OH)_2$ of as-cast and solution heat-treated binary Mg-X alloys: X = Mn, Sn, Ca, Zn, Al, Zr, Si, Sr, Corros. Sci. 76 (2013) 60–97.
[17] Z. Shi, M. Liu, A. Atrens, Measurement of the corrosion rate of magnesium alloys using Tafel extrapolation, Corros. Sci. 52 (2010) 579–588.
[18] G. Song, A. Atrens, Corrosion mechanisms of magnesium alloys, Adv. Eng. Mater. 1 (1999) 11–33.
[19] G. Song, A. Atrens, Understanding magnesium corrosion – a framework for improved alloy performance, Adv. Eng. Mater. 5 (2003) 837–858.
[20] G. Song, Recent progress in corrosion and protection of magnesium alloys, Adv. Eng. Mater. 7 (2005) 563–586.
[21] H. Matsubar, Y. Ichige, K. Fujita, H. Nishiyama, K. Hodouchi, Effect of impurity Fe on corrosion behavior of AM50 and AM60 magnesium alloys, Corros. Sci. 66 (2013) 203–210.
[22] G.R. Meira, C. Andrade, C. Alonso, I.J. Padaratz, J.C. Borba, Salinity of marine aerosols in a Brazilian coastal area-Influence of wind regime, Atmos. Environ. 41 (2007) 8431–8441.
[23] Z. Cui, X. Li, K. Xiao, C. Dong, Atmospheric corrosion of field-exposed AZ31 magnesium in a tropical marine environment, Corros. Sci. 76 (2013) 243–256.
[24] J. Liao, M. Hotta, S. Motoda, T. Shinohara, Atmospheric corrosion of two field-exposed AZ31B magnesium alloys with different grain size, Corros. Sci. 71 (2013) 53–61.
[25] L. Yang, Y. Li, Y. Wei, L. Hou, Y. Tian, Atmospheric corrosion of field-exposed AZ91D Mg alloys in a polluted environment, Corros. Sci. 52 (2010) 2188–2196.
[26] Y.G. Li, Y.H. Wei, L.F. Hou, P.J. Han, Atmospheric corrosion of AM60 Mg alloys in an industrial city environment, Corros. Sci. 69 (2013) 67–76.
[27] R. Lindström, On chemistry of atmospheric corrosion, Doctoral thesis, Department of Chemistry, Göteborg University, Göteborg, 2003.
[28] D.B. Blücher, J.E. Svensson, L.G. Johansson, M. Rohwerder, M. Stratmann, Scanning kelvin probe force microscopy, a useful tool for studying atmospheric corrosion of Mg–Al alloys in situ, J. Electrochem. Soc. 151 (2004) B621–B626.
[29] M. Shahabi, M. Esmaily, J.E. Svensson, M. Halvarsson, L. Nyborg, Y. Cao, L.G. Johansson, The influence of CO_2 on NaCl-induced atmospheric corrosion of the MgAl alloy AM50, J. Electrochem. Soc. 161 (2014) C277–C287.
[30] N. LeBozec, M. Jonsson, D. Thierry, Atmospheric corrosion of magnesium alloys: influence of temperature, relative humidity, and chloride deposition, Corrosion 60 (2004) 356–361.
[31] C. Lin, X. Li, Role of CO_2 in the initial stage of atmospheric corrosion of AZ91 magnesium alloy in the presence of NaCl, Rare Met. 25 (2006) 190–196.
[32] S. Feliu, A. Pardo, M.C. Merino, A.E. Coy, F. Viejo, R. Arrabal, Correlation between the surface chemistry and the atmospheric corrosion of AZ31, AZ80 and AZ91D magnesium alloys, Appl. Surf. Sci. 255 (2009) 4102–4108.
[33] M. Jönsson, D. Persson, R. Gubner, The initial steps of atmospheric corrosion on magnesium alloy AZ91D, J. Electrochem. Soc. 154 (2007) C684–C691.
[34] M. Jönsson, D. Persson, C. Leygraf, Atmospheric corrosion of field-exposed magnesium alloy AZ91D, Corros. Sci. 50 (2008) 1406–1413.
[35] S. Feliu, C. Maffiotte, J.C. Galván, V. Barranco, Atmospheric corrosion of magnesium alloys AZ31 and AZ61 under continuous condensation conditions, Corros. Sci. 53 (2011). 1865-1827.
[36] R. Arrabal, E. Matykina, A. Pardo, M.C. Merino, K. Paucar, M. Mohedano, P. Casajús, Corrosion behaviour of AZ91D and AM50 magnesium alloys with Nd and Gd additions in humid environments, Corros. Sci. 55 (2012) 351–362.
[37] D.B. Blücher, J.E. Svensson, L.G. Johansson, The NaCl-induced atmospheric corrosion of aluminum: the influence of carbon dioxide and temperature, J. Electrochem. Soc. 150 (2003) B93–B98.
[38] A. Niklasson, L.G. Johansson, J.E. Svensson, The influence of relative humidity and temperature on the acetic acid vapour-induced atmospheric corrosion of lead, Corros. Sci. 50 (2008) 3031–3037.
[39] J.E. Svensson, L.G. Johansson, The temperature-dependence of the SO_2-induced atmospheric corrosion of zinc; a laboratory study, Corros. Sci. 38 (1996) 2225–2233.
[40] J. Chen, J.Q. Wang, E.H. Han, W. Ke, Effect of temperature on initial corrosion of AZ91 magnesium alloy under cyclic wet-dry conditions, Corr. Eng. Sci. Technol. 46 (2011) 267–277.
[41] J. Balej, Water vapour partial pressures and water activities in potassium and sodium hydroxide solutions over wide concentration and temperature ranges, Int. J. Hydro. Energy 10 (1985) 233–243.
[42] R.M. Wang, A. Eliezer, E.M. Gutman, An investigation on the microstructure of an AM50 magnesium alloy, Mater. Sci. Eng., A 355 (2003) 201–207.
[43] C.B. Baliga, P. Tsakiropoulos, Development of corrosion resistant magnesium alloys: Part 2. Structure of corrosion products on rapidly solidified Mg–16Al alloys, Mater. Sci. Technol. 9 (1993) 513–519.
[44] X. Guo, J. Chang, S. He, W. Ding, X. Wang, Investigation of corrosion behaviors of Mg–6Gd–3Y–0.4Zr alloy in NaCl aqueous solutions, Electrochim. Acta 52 (2007) 2570–2577.
[45] R.A. Robinson, R.H. Stokes, Electrolyte Solutions, Butterworths, London, 1965.
[46] K.S. Pitzer, Thermodynamics of electrolytes, II. Activity and osmotic coefficients with one or both ions univalent, J. Phys. Chem. 77 (1973) 268–277.
[47] R.J. Bodnar, Revised equation and table for determining the freezing point depression of H_2O–NaCl solutions, Geochim. Cosmochim. Acta 57 (1993) 683–684.
[48] G. Baril, N. Pebere, The corrosion of pure magnesium in aerated and deaerated sodium sulphate solutions, Corros. Sci. 43 (2001) 471–484.
[49] W. Song, H.J. Martin, A. Hicks, D. Seely, C.A. Walton, W.B. Lawrimore, P.T. Wang, M.F. Horstemeyer, Corrosion behaviour of extruded AM30 magnesium alloy under salt-spray and immersion environments, Corros. Sci. 78 (2014) 353–368.
[50] E. Gulbrandsen, Anodic behaviour of Mg in HCO_3^-/CO_2^{-3} buffer solutions. Quasi-steady measurements, Electrochim. Acta 37 (1992) 1403–1412.
[51] M.J. Blandamer, J.B. Engberts, P.T. Gleeson, J.C. Reis, Activity of water in aqueous systems; a frequently neglected property, Chem. Soc. Rev. 34 (2005) 440–458.
[52] J.E. Svensson, L.G. Johansson, A laboratory study of the initial stages of the atmospheric corrosion of zinc in the presence of NaCl; influence of SO_2 and NO_2, Corros. Sci. 34 (1993) 721–740.
[53] S. Takigawa, I. Muto, N. Hara, Corrosion in marine and saltwater environments, in: ECS Transactions, 214th ECS Meeting, 2009, pp. 71–80.